Journal of Materials Science: Materials in Electronics (2018) 29:7842–7850
https://doi.org/10.1007/s10854-018-8783-z

# Fabrication and enhanced dielectric properties of polyimide matrix composites with core–shell structured $CaCu_3Ti_4O_{12}$@$TiO_2$ nanofibers

**Junchuan Wang[1] · Yunchen Long[1] · Ying Sun[1] · Xueqin Zhang[1] · Hong Yang[1] · Baoping Lin[1]**

Received: 20 December 2017 / Accepted: 16 February 2018 / Published online: 22 February 2018


**Abstract**
Core–shell structured $CaCu_3Ti_4O_{12}$@$TiO_2$ (CCTO@$TiO_2$) nanofibers were prepared via a normal coaxial electrospinning technique with sol precursors. Polyimide (PI) nanocomposite films containing the core–shell structured CCTO@$TiO_2$ nanofibers were fabricated by the solution casting method. The core–shell structure of the CCTO@$TiO_2$ nanofibers was confirmed through transmission electron microscope. The percolation of the CCTO/$TiO_2$ interfaces leads to much enhanced interfacial polarization of the CCTO@$TiO_2$ nanofibers, which gives rise to substantially increased dielectric constant of the nanocomposites. Compared to the nanocomposites with CCTO nanofibers, the breakdown strength of the nanocomposites with CCTO@$TiO_2$ nanofibers is also increased due to the charge shifting is limited to the interfacial zone of CCTO/$TiO_2$ interfaces, instead of in the PI matrix to form a percolation path. For the nanocomposites with 5 vol% nanofibers, the dielectric constant of 5.55 was enhanced to 5.85 and the breakdown strength of 201 kV/mm was increased to 236 kV/mm by utilizing the $TiO_2$ coated CCTO nanofibers, while the dielectric loss shows no obvious change. Meanwhile, the PI nanocomposite film filled with 1 vol% CCTO@$TiO_2$ nanofibers exhibits a maximal energy density of 1.6 J/cm$^3$. The core–shell structured nanofibers open up an effective way to optimize the dielectric properties of polymer nanocomposites with high energy density.

## 1 Introduction

Polymeric matrix composites with high dielectric permittivity, low dielectric loss and high breakdown strength have received tremendous attentions because of their widely range of applications in energy storage, electronic fields and organic thin film transistors [1–9]. Compared with traditional inorganic dielectric materials, the polymeric matrix composites are more potential because of their excellent performance such as good flexibility, processability and dielectric strength. Polyimide (PI) is one of the candidates due to its good thermal stability, low moisture absorption, ease of film preparation and good mechanical properties [10, 11]. However, most polymers are originally low dielectric constant which fail to meet the requirement of dielectric performance. Thus, developing polymer matrix composites with high dielectric constant can be a promising alternative to solve the problem.

Generally, there are two possible ways to increase the dielectric permittivity of polymers. One strategy is to introduce conductive nanofillers (e.g., Ag particles, carbon fibers, carbon nanotube and polyaniline) into polymers [12–18]. Ultrahigh dielectric constant can be achieved for these polymeric matrix composites but with a few defects such as a relatively high conductivity, high loss tangent and low breakdown strength when little concentration of conductive nanofillers were added. Another approach is adding ceramic nanofillers with high dielectric permittivity such as $TiO_2$, $ZrO_2$, $BaTiO_3$ (BT), and $CaCu_3Ti_4O_{12}$ (CCTO) into polymers [19–30]. Unfortunately, the ceramic/polymer composites need a large nanofiller loading (50 vol%) to get a high dielectric constant, which results in the composites lose their advantages such as low dielectric loss, high breakdown strength, flexibility and uniformity. The stored energy density (Uc) of a dielectric material is expressed as $Uc = \int EdD$, where D is the electric displacement and E is the applied electric field [31]. Therefore, to increase the maximum Uc of dielectric materials, it is extremely important to develop dielectric materials with maximal applied electric field it can be applied and high dielectric permittivity which is related to the electric displacement.

✉ Baoping Lin
lbp@seu.edu.cn

[1] School of Chemistry and Chemical Engineering, Southeast University, Nanjing 211189, Jiangsu, People's Republic of China

Theoretical calculation and experimental studies have found the dielectric nanofibers with a high aspect ratio can increase the dielectric constant as well as breakdown strengths effectively at a low concentrations (1–5 vol%), which breaks the paradox of high dielectric constant with decreased breakdown strength [32–35]. The nanofibers could effectively reduce the surface energy and prevent their aggregation in the polymeric matrix composites, which contributes to the enhanced breakdown strengths. However, the breakdown strength of nanocomposites still decreased with high loading of nanofibers, due to the more structure imperfections and electric field concentration exist at the interface between the nanofibers and the polymeric matrix composites.

Interface polarization is the dominant mechanism of polarization in the polymeric matrix nanocomposites. To modulate the interface polarization, nanofibers with core–shell structure were imported to realize it. Generally, high permittivity nanofibers coated with an inorganic buffer layer with moderate permittivity, can effectively reduce the local electric field and moderate the interfacial polarization in the polymer matrix [36]. Recently, some studies showed that the nanofibers with core–shell structure have effectively increased the energy density of nanocomposites. Zhang et al. found the energy density of polyvinylidene fluoride (PVDF) nanocomposite can be enhanced to 31.2 J/cm$^3$ by the $TiO_2$ nanofiber embedded $BaTiO_3$ nanoparticles [37]. Liu et al. demonstrated that the discharged energy density of PVDF nanocomposite film could be significantly improved to 7.1 J/cm$^3$ by the incorporation of $BaTiO_3$@$Al_2O_3$ [32]. Our group demonstrated that the energy density of the PI nanocomposites increased to 2.31 J/cm$^3$ containing a low volume fraction of core–shell structured $BaTiO_3$@$SiO_2$ nanofibers. The energy density of PI nanocomposites could be markedly enhanced by introducing the $SiO_2$ shell on the surface of $BaTiO_3$ nanofibers [38].

Along this line, a core–shell structure of $CaCu_3Ti_4O_{12}$@$TiO_2$ (CCTO@$TiO_2$) nanofibers has been designed and prepared via coaxial electrospinning. The PI nanocomposite films consisting of the core–shell structured CCTO@$TiO_2$ have been successfully synthesized by the solution casting method (Scheme 1). Compared with the CCTO/PI nanocomposites, the dielectric constant as well as the breakdown strength is highly enhanced in the CCTO@$TiO_2$/PI nanocomposites. In addition, the nanocomposite with a 1 vol% of CCTO@$TiO_2$ nanofibers raised the breakdown strength up to 299 kV/mm, which exhibits the maximal energy density of 1.6 J/cm$^3$. This work shows the advantage of the core–shell nanofiber in enhancing the dielectric permittivity of polymeric matrix composites, and presents a novel strategy to efficiently increase the energy density.

## 2 Experimental

### 2.1 Preparation of the CCTO@$TiO_2$ nanofibers

CCTO@$TiO_2$ nanofibers were prepared by a normal coaxial electrospinning technique. Raw calcium nitrate terahydrate, copper acetate monohydrate and tetrabutyl titanate (TNBT) in a 1:3:4 target molar ratio were dissolved in ethanol with stirring to obtain a uniform precursor solution. Polyvinylpyrrolidone (M ~ 1,300,000) was used to control the sol viscosity of the solution. The TNBT sol solution was obtained through the same procedure. Then the two sol solutions were respectively transferred into two syringes. The coaxial electrospinning process was realized at electric field of 1.8 kV/cm. The as-electrospun nanofibers were calcined at 850 °C for 3 h to obtained CCTO@$TiO_2$ nanofibers. To effectively improve the compatibility between the PI matrix and the nanofibers, dopamine was introduced into surface of the CCTO@$TiO_2$ nanofibers. The CCTO nanofibers and CCTO@$TiO_2$ nanofibers were respectively ultrasonic

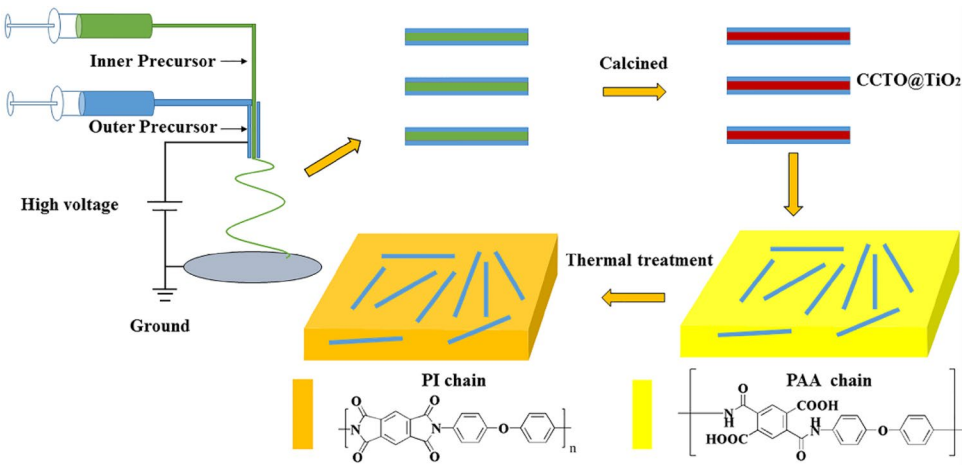


**Scheme 1** The fabrication procedures of CCTO@$TiO_2$/PI nanocomposite films

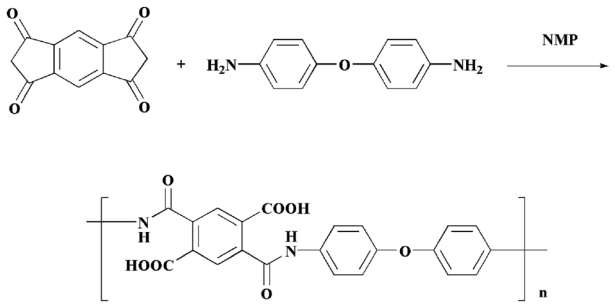


**Scheme 2** Synthetic route for PAA

dispersed into 0.01 mol/L dopamine hydrochloride aqueous solution with stirring at 60 °C for 12 h. Then the dopamine-coated nanofibers were obtained by centrifugation and dried at 100 °C for 6 h.

### 2.2 Synthesis of polyamic acid (PAA)

The synthesis of PAA is shown in Scheme 2. Firstly, a certain amount of recrystallized diamino diphenyl ether (ODA) was added into the distilled NMP and stirred under the protection of nitrogen atmosphere and an ice bath. As ODA was fully dissolved in the NMP, pyromellitic dianhydride was added into the solution for three times. At last, the solution was stirred for 24 h to get the PAA solution with a content of 0.1 g/mL preserved in a desiccator for use.

### 2.3 Fabrication of the nanocomposite films

The nanocomposite films were prepared as follows. To form a homogeneous suspensions, the dopamine-coated CCTO@$TiO_2$ nanofibers and PAA solution were proportionally ultrasonic dispersed in NMP, and then stirred for 24 h. The suspensions were poured into a glass mold and as-cast films were progressively dried at 60 °C for 2 h, 90 °C for 2 h, 120 °C for 2 h, 150 °C for 2 h, 180 °C for 2 h and 240 °C for 1 h. In the end, the films were transferred into a muffle furnace to completely imidize at 300 °C for 2 h. A series of PI based composite films (PI-1, PI-2, PI-3, PI-4 and PI-5) of different CCTO@$TiO_2$ nanofibers contents (1, 2, 3, 4 and 5 vol%) were fabricated. For comparison, CCTO/PI composite films (PI–CCTO-1, PI–CCTO-2, PI–CCTO-3, PI–CCTO-4 and PI–CCTO-5) also were prepared by the same process as above. The thickness of the final nanocomposite films is ≈ 15 μm.

### 2.4 Characterization

X-ray diffraction (XRD) patterns were performed with a Bruker D8 Advance X-ray diffractometer using Cu Kα radiation (40 kV, 200 mA). Fourier transform Infrared (FTIR) transmission spectra were performed with a BRUKER-EQUINOX-55 IR spectrophotometer. The thermogravimetric analysis (TGA) was tested on TA Instruments SDT-Q600 with a heating rate of 20 °C/min and a nitrogen atmosphere with a gas flow rate of 100 mL/min. The microstructure of CCTO@$TiO_2$ nanofibers was observed by a transmission electron microscope (TEM, Tecnai, and G2 T20). The morphologies of the cross-section and the in-plane of nanocomposite film were observed with a Hitachi S-4800 scanning electron microscope (SEM). X-ray photoelectron spectroscopy (XPS) measurements were performed with a Thermo Scientific K-Alpha using monochromatic Al Kα radiation. The dielectric permittivity and dielectric loss of the nanocomposite film were measured using a Hioki 3532-50 impedance analysis instrument (Ueda, Nagano, Japan) with a frequency range from $10^3$ to $10^7$ Hz at room temperature. Electric breakdown tests were carried out with the Dielectric Breakdown Voltage Test (HCDJC-50 kV, Beijing Hua Ce Testing Instrument Co., Ltd, China) at a climbing speed of 200 V/s[1] and a limited current of 5 mA.

## 3 Results and discussion

### 3.1 Microstructure and characterization of CCTO@$TiO_2$ nanofiber

The CCTO@$TiO_2$ nanofibers were successfully prepared by the normal coaxial electrospinning method. Figure 1 demonstrates the XRD pattern of the CCTO@$TiO_2$ nanofibers. According to the standard PDF card, the nanocomposite phases of perovskite CCTO and rutile $TiO_2$ are well indexed. The morphology and structure of the CCTO@$TiO_2$ nanofiber were further determined by the SEM and TEM images. The ceramic CCTO@$TiO_2$ nanofibers are uniform in appearance and have a high aspect ratio, with a diameter

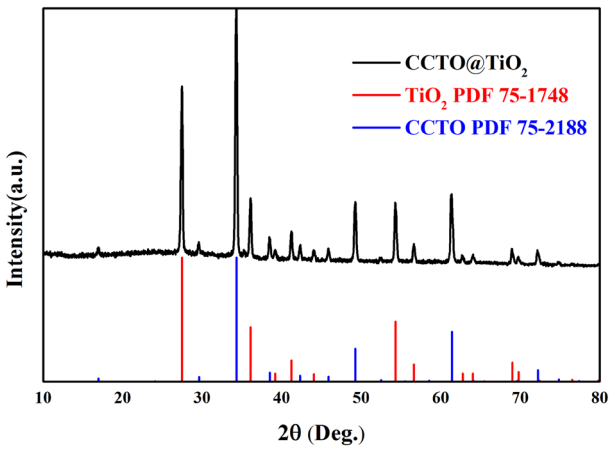


**Fig. 1** XRD pattern of the heat-treated CCTO@$TiO_2$ nanofibers

of 350 nm and length of a few dozens of micrometer. As demonstrated in Fig. 2b, the CCTO@$TiO_2$ nanofiber has an apparent core–shell structure, where the thickness of the outer shell layer is approximately 20 nm and the inner core layer is 300 nm.

For further improve the compatibility between CCTO@$TiO_2$ nanofibers and pristine PI matrix, dopamine are employed as the surface functionalization of the CCTO@$TiO_2$ nanofibers. This can be further evidenced by FTIR and XPS. Figure 3a presents the results of FTIR of raw CCTO nanofibers, CCTO@$TiO_2$ nanofibers and dopamine-coated CCTO@$TiO_2$ nanofibers. Successful modification by dopamine of CCTO@$TiO_2$ nanofibers is confirmed by new absorbance peaks appeared at 1480 and 1260 cm, which respectively are correspond to aromatic C–C stretching vibrations and aromatic amine C–N stretching vibrations, however such peaks are not observed in the matter of unmodified CCTO@$TiO_2$ nanofibers. Figure 3b exhibits the results of XPS of raw CCTO nanofibers, CCTO@$TiO_2$ nanofibers and dopamine-coated CCTO@$TiO_2$ nanofibers. Compared with CCTO and CCTO@$TiO_2$ nanofibers, the peak of N 1s at about 400 eV which is owing to free –$NH_2$ is observed at dopamine-coated CCTO@$TiO_2$ nanofibers, affirming the successfully introduction of dopamine on the CCTO@$TiO_2$ nanofibers surface.

### 3.2 Microstructure and characterization of CCTO@$TiO_2$/PI nanocomposite films

The XRD patterns of PI, CCTO@$TiO_2$/PI composites with the nanofibers contents of 1, 2, 3, 4 and 5 vol% are shown in Fig. 4. It can be found that the positions and relative intensities of the PI nanocomposite films are in good agreement with CCTO@$TiO_2$ nanofibers after them were incorporated into PI matrix. As the volume fraction of CCTO@$TiO_2$ nanofibers increasing, the peaks of the perovskite CCTO and rutile $TiO_2$ became sharper and stronger, while the signal of PI reduced gradually. In addition, the XRD patterns of

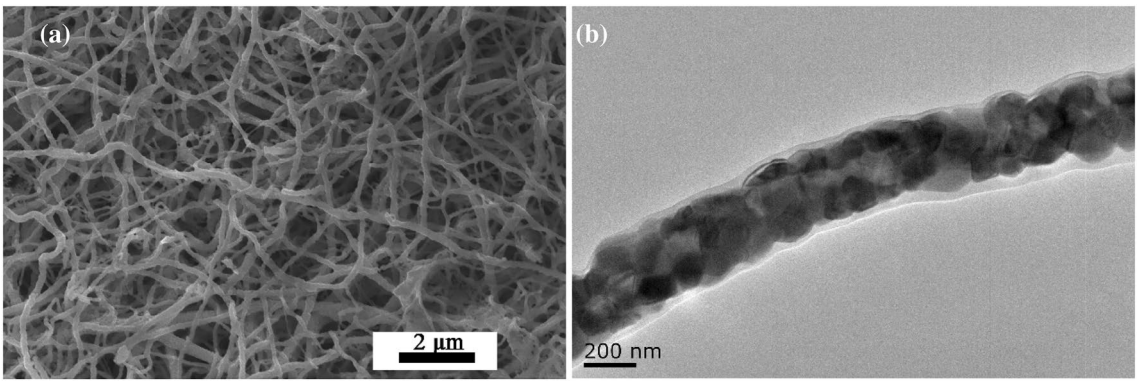


**Fig. 2** The microstructures of CCTO@$TiO_2$ nanofibers: **a** SEM image of CCTO@$TiO_2$ nanofibers and **b** TEM image of CCTO@$TiO_2$ nanofibers

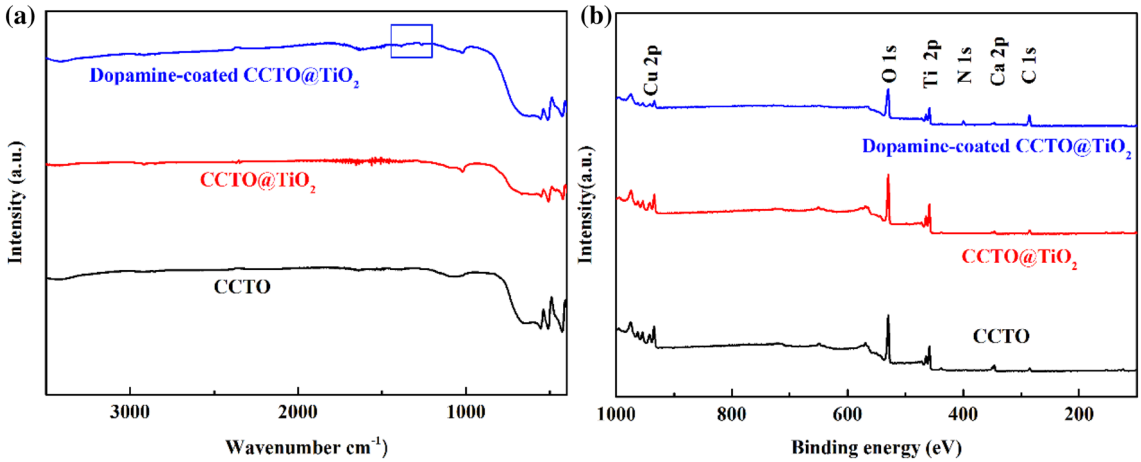


**Fig. 3** **a** FTIR spectra, **b** XPS spectra of CCTO nanofibers, CCTO@$TiO_2$ nanofibers and dopamine-coated CCTO@$TiO_2$ nanofibers

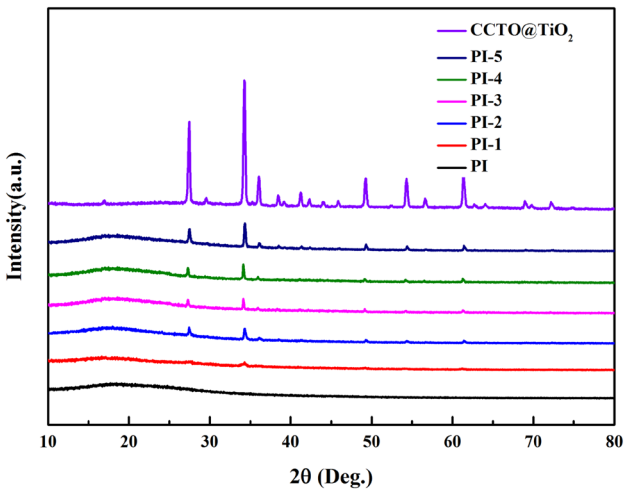


**Fig. 4** XRD pattern of CCTO@$TiO_2$ nanofibers and CCTO@$TiO_2$/PI nanocomposite films

the PI based nanocomposites show the CCTO, $TiO_2$, and PI diffraction peaks and clearly showed that the CCTO@$TiO_2$ nanofibers are filled in the polymer matrix.

Figure 5 shows the morphologies and microstructures of the pristine PI and the 5 vol% CCTO@$TiO_2$/PI nanocomposite film. As showed in Fig. 5a, b, the surface of pristine PI is neat and smooth and there is not pores or voids in the fracture surface. Figure 5c, d exhibit the CCTO@$TiO_2$ nanofibers are randomly and uniformly distributed into the PI based nanocomposites, meanwhile there is not agglomeration and voids observed for the film. The majority of the embedded CCTO@$TiO_2$ nanofibers remains in a high aspect ratio, which has a significant impact on the dielectric property.

### 3.3 Dielectric properties of the nanocomposite films

The dielectric properties of the PI nanocomposites as a function of frequency and the CCTO@$TiO_2$ nanofibers volume fraction is researched. Figure 6 demonstrates the frequency dependence of dielectric properties of PI based nanocomposite films. Obviously, the dielectric permittivity gradually increases with the addition of CCTO@$TiO_2$ nanofibers in the whole testing frequency range. For the content of CCTO@$TiO_2$ nanofibers is 5 vol%, the dielectric constant of the nanocomposite film is 5.85, which is substantially enhanced by 70% over that of pristine PI (3.40). The dielectric constant of the PI nanocomposite films has a

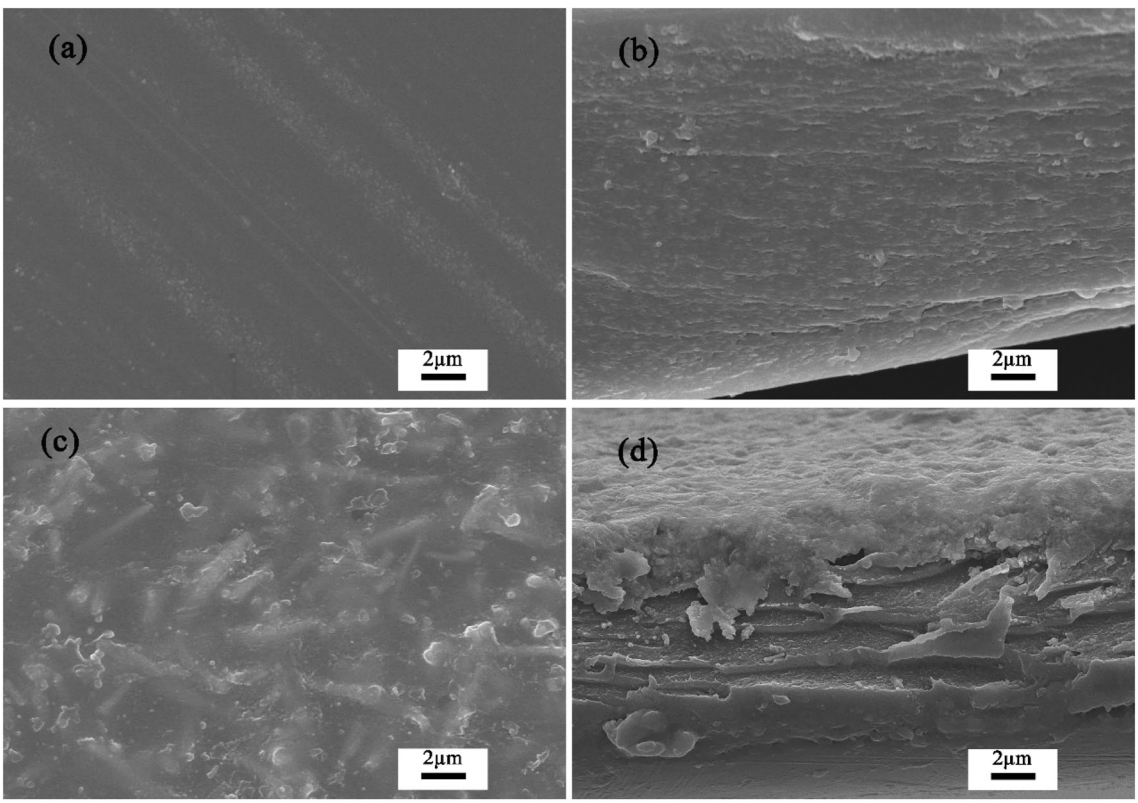


**Fig. 5** **a** Surface and **b** cross-section SEM images of pristine PI; **c** surface and **d** cross-section SEM images of 5 vol% CCTO@$TiO_2$/PI nanocomposite films

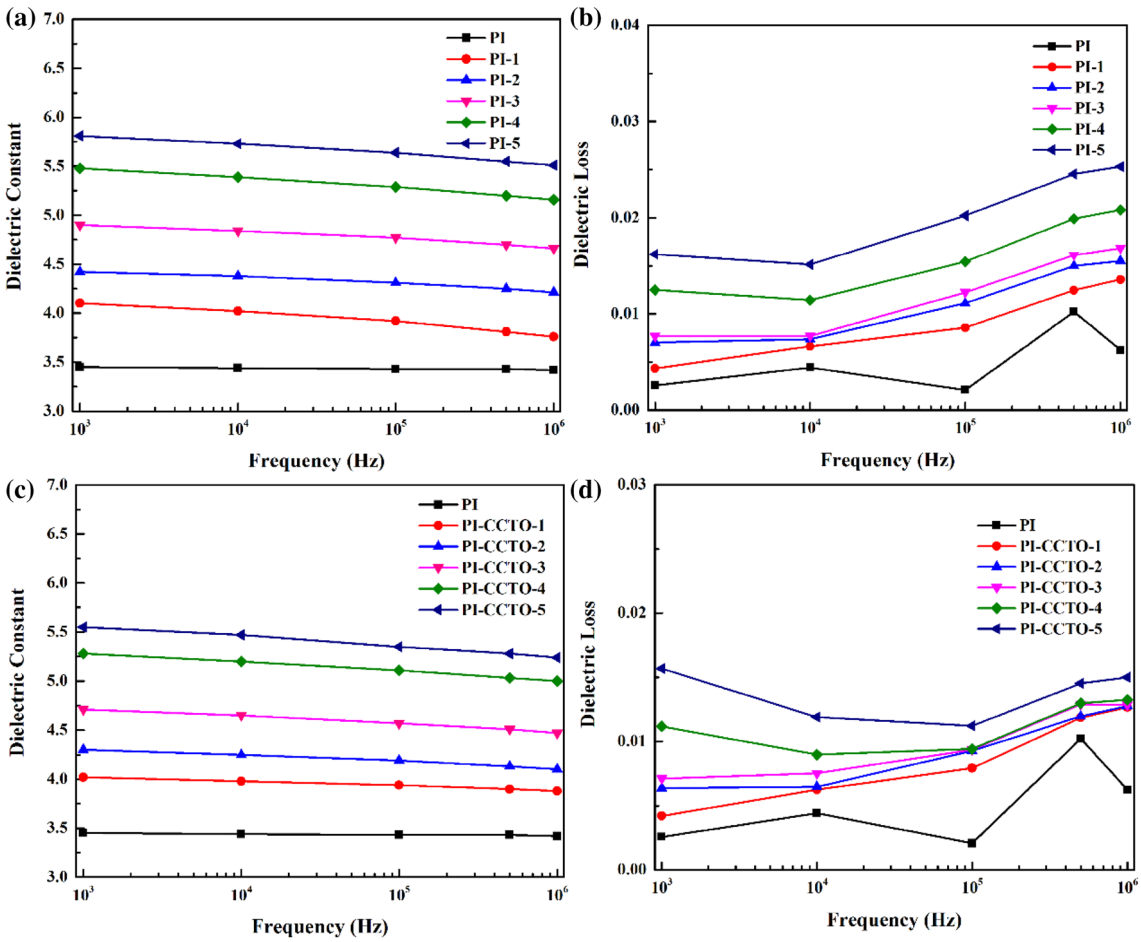


**Fig. 6** Frequency-dependence of the **a** dielectric constant and **b** dielectric loss of CCTO@$TiO_2$/PI nanocomposite films and frequency-dependence of the **c** dielectric constant and **d** dielectric loss of CCTO/PI nanocomposite films

great improvement mainly originated from the introduction of high dielectric constant CCTO@$TiO_2$ nanofibers.

In addition, for the high-performance dielectric materials, dielectric loss is another important parameter that needs to be considered. Figure 6b, d shows the dependence of frequency on the dielectric loss of PI based nanocomposites. The dielectric loss of the CCTO@$TiO_2$/PI nanocomposite films is ranging from 0.0021 to 0.025. Even the loading content of CCTO@$TiO_2$ nanofibers is increased to 5 vol%, the dielectric loss is only 0.025, which is quite low compared with other traditional nanocomposites.

To availably show the effect of the core–shell structure on the dielectric properties of the PI nanocomposites, CCTO nanofibers without $TiO_2$ coating were fabricated. Figure 7 demonstrate the comparison of the dielectric permittivity and dielectric loss between nanocomposites with CCTO nanofibers and nanocomposites with CCTO@$TiO_2$ nanofibers, respectively. It is clearly demonstrated that by creating the core–shell structure, the nanocomposites with CCTO@$TiO_2$ nanofibers showed a significant increase in the

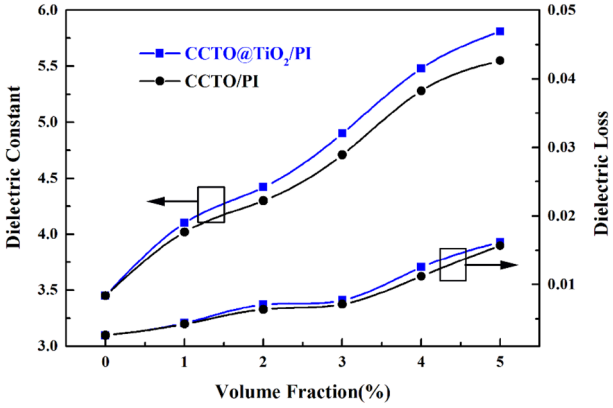


**Fig. 7** Dependence of the dielectric constant and dielectric loss of the CCTO@$TiO_2$/PI and CCTO/PI nanocomposite films on the volume fraction, measured at room temperature and 1 kHz

dielectric permittivity meanwhile maintaining a low dielectric loss. For the nanocomposites with 5 vol% CCTO@$TiO_2$ nanofibers, the dielectric constant of 5.55 was enhanced to 5.85 by utilizing the $TiO_2$ coated CCTO nanofibers, while the dielectric loss shows no obvious change. The CCTO@$TiO_2$ nanofibers are quite efficient at increasing the dielectric constant of the nanocomposites. The primary improvement is attributed to the percolation of the CCTO/$TiO_2$ interfaces leads to much enhanced interfacial polarization of the CCTO@$TiO_2$ nanofibers, which gives rise to substantially increased dielectric constant of the nanocomposites.

### 3.4 Breakdown strength and energy storage of the nanocomposite films

The energy density (Uc) is depended on the electric displacement (D) and applied electric field (E) of the dielectrics as: $Uc = \int EdD$. The electric displacement (D) is determined by relative dielectric constants ($\varepsilon_r$) and the polarization (P) by $D = P + \varepsilon_r\varepsilon_0 E$, where $\varepsilon_0$ is the vacuum permittivity. For liner dielectrics, $Uc = 1/2\ \varepsilon_r\varepsilon_0 E_b^2$, where $E_b$ is the breakdown strength of the dielectrics [39]. Thus, for dielectric materials, the breakdown strength is the most critical parameter in defining the energy density of nanocomposites in electrostatic capacitor application. Figure 8 exhibits the breakdown strength of PI based nanocomposites with varying contents of CCTO nanofibers and CCTO@$TiO_2$ nanofibers. The results declare that the breakdown strength of the nanocomposites with CCTO@$TiO_2$ nanofibers is higher than those of CCTO nanofibers at the same volume fraction. Such as, at 5 vol% of nanofibers, the breakdown strength of the composite with CCTO@$TiO_2$ nanofibers is 236 kV/mm, about 1.2 times that of the CCTO nanofibers (201 kV/mm). Compared to the nanocomposites with CCTO nanofibers, the breakdown strength of the nanocomposites with CCTO@$TiO_2$ nanofibers is enhanced due to the charge shifting is subjected to the interfacial zone of CCTO/$TiO_2$ interfaces, instead of in the PI matrix to form a percolation path. Compared to pristine PI, increasing the content of CCTO@$TiO_2$ nanofibers in PI nanocomposites results in continuous decrease of breakdown strength, such as for 5 vol% of CCTO@$TiO_2$ nanofibers, the breakdown strength decreases to 236 kV/mm, which is generally related to the structural defects, such as voids or pores, caused by the introduction of increasing amounts of nanofibers.

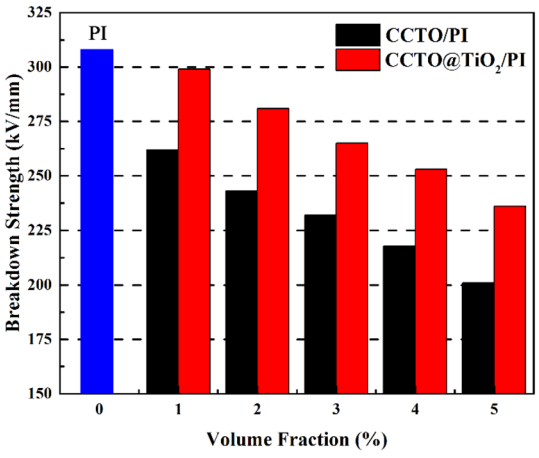


**Fig. 8** Breakdown strength comparison for CCTO/PI nanocomposites and CCTO@$TiO_2$/PI nanocomposites

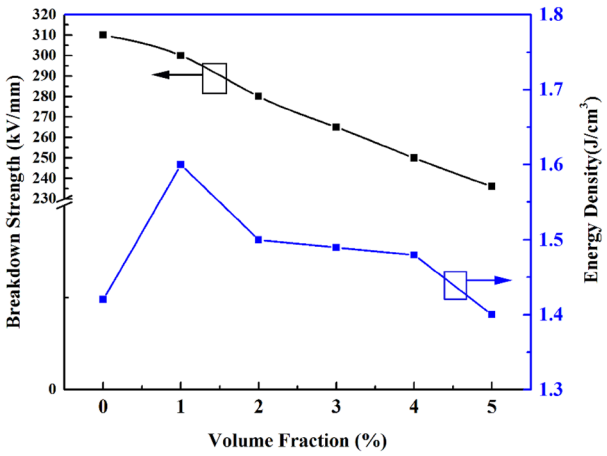


**Fig. 9** Dielectric breakdown strength and energy density of CCTO@$TiO_2$/PI nanocomposite films with different volume fractions

The energy storage density of PI based composites containing various volume fractions of modified CCTO@$TiO_2$ nanofibers as a function of breakdown strength is presented in Fig. 9. As the content of CCTO@$TiO_2$ nanofibers increases, the maximum energy storage density of the

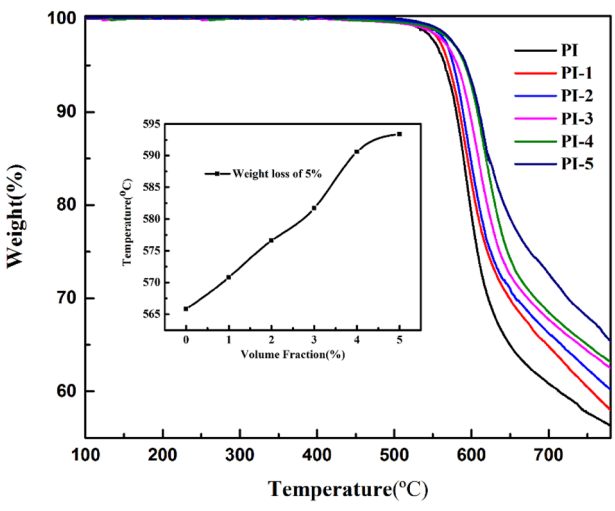


**Fig. 10** TGA of the CCTO@$TiO_2$/PI nanocomposite films and pristine PI at a nitrogen atmosphere. The insight is the weight loss of 5% of pristine PI and CCTO@$TiO_2$/PI nanocomposite films

**Table 1** Weight loss of 5% of pristine PI and the CCTO@$TiO_2$/PI nanocomposite films

| Sample | PI | PI-1 | PI-2 | PI-3 | PI-4 | PI-5 |
|---|---|---|---|---|---|---|
| Weight loss of 5% (°C) | 565.8 | 570.8 | 576.6 | 581.7 | 590.6 | 593.4 |

composite films first increases obviously, and then decreases with the increase of CCTO@$TiO_2$ nanofibers content in the composite films. The maximum energy storage density of the nanocomposites with 1 vol% of CCTO@$TiO_2$ nanofibers reaches a value as high as 1.6 J/cm$^3$ at 299 kV/mm, which is more than 14% increases compared with the pristine PI of 1.4 J/cm$^3$ at 308 kV/mm.

### 3.5 Thermal properties of the nanocomposite films

Figure 10 shows TGA curves of the PI based composite films containing CCTO@$TiO_2$ nanofibers at a nitrogen atmosphere. Thermal stability of the PI nanocomposite films is of prime importance for high temperature applications. As indicated in Fig. 10, the CCTO@$TiO_2$/PI nanocomposite films have good thermal stability below 500 °C and there is not weight loss for all the PI nanocomposite films. Table 1 shows the weight loss temperatures (> 5% weight loss) of PI, PI-1, PI-2, PI-3, PI-4 and PI-5 are 565.8, 570.8, 576.6, 581.7, 590.6 and 593.4 °C, respectively. Therefore, it could be concluded that the CCTO@$TiO_2$ nanofibers gives rise to greater thermal stability of the PI nanocomposite films. The CCTO@$TiO_2$ nanofibers have larger specific surface area, potentially leading to the improved interfacial fiber/PI interaction which will restrict the thermal motion of PI chains, thus resulting in much higher thermal properties of the CCTO@$TiO_2$/PI nanocomposite films.

## 4 Conclusions

In conclusion, CCTO@$TiO_2$ nanofibers were successfully fabricated by the normal coaxial electrospinning method. The TEM images exhibited that $TiO_2$ was homogeneously coated on the surface of CCTO nanofibers with an average thickness of 20 nm. The PI nanocomposite films consisting of 1D core–shell structured CCTO@$TiO_2$ nanofibers have been successfully fabricated through the solution casting method. The SEM images demonstrated that the CCTO@$TiO_2$ nanofibers were uniformly dispersed in the PI matrix. The TGA results indicated that the CCTO@$TiO_2$/PI nanocomposite films have excellent thermal stability below 500 °C. The nanocomposites of CCTO@$TiO_2$ nanofibers exhibit higher dielectric constant and enhanced breakdown strength compared to those of CCTO nanofibers. For the nanocomposites with 5 vol% CCTO@$TiO_2$ nanofibers, the dielectric constant of 5.55 was enhanced to 5.85 and the breakdown strength of 201 kV/mm was increased to 236 kV/mm by utilizing the $TiO_2$ coated CCTO nanofibers, while the dielectric loss shows no obvious change. In addition, the energy density of the composites with 1 vol% CCTO@$TiO_2$ nanofibers exhibits a maximal energy density of 1.6 J/cm$^3$, which is more than 14% increases compared with the pristine PI of 1.4 J/cm$^3$. The core–shell structured nanofibers are effective in increasing the dielectric constant as well as the breakdown strength to enhance the energy storage density of polymer composites.

**Acknowledgements** This study was financially supported by National Natural Science Foundation of China (21304018 and 21374016), Jiangsu Provincial Natural Science Foundation of China (BK20130619 and BK20130617) and a project funded by the Priority Academic Program Development of Jiangsu Higher Education Institutions.

## References

1. B. Chu, X. Zhou, K. Ren, B. Neese, M. Lin, Q. Wang, F. Bauer, Q.M. Zhang, Science **313**, 334 (2006)
2. E.J. Barshaw, J. White, M.J. Chait, J.B. Cornette, J. Bustamante, F. Folli, D. Biltchick, G. Borelli, G. Picci, M. Rabuffi, IEEE Trans. Magn. **43**, 223 (2007)
3. T. Tanaka, M. Kozako, N. Fuse, Y. Ohki, IEEE Trans. Dielectr. Electr. Insul. **12**, 669 (2005)
4. Y. Hirose, K. Adachi, Macromolecules **39**, 1779 (2006)
5. R.A.C. Amoresi, A.A. Felix, E.R. Botero, N.L.C. Domingues, E.A. Falcao, M.A. Zaghete, A.W. Rinaldi, Ceram. Int. **41**, 14733 (2015)
6. E. Baer, L. Zhu, Macromolecules **50**, 2239 (2017)
7. W. Xia, Z. Xu, F. Wen, Z. Zhang, Ceram. Int. **38**, 1071 (2012)
8. Q. Li, G. Zhang, F. Liu, K. Han, M.R. Gadinski, C. Xiong, Q. Wang, Energy Environ. Sci. **8**, 922 (2015)
9. H. Zhu, Z. Liu, F. Wang, J. Mater. Sci. **52**, 50489 (2017)
10. Y. Chen, B. Lin, X. Zhang, J. Wang, C. Lai, Y. Sun, Y. Liu, H. Yang, J. Mater. Chem. A **2**, 14118 (2014)
11. X. Fang, X. Liu, Z.K. Cui, J. Qian, J. Pan, X. Li, Q. Zhuang, J. Mater. Chem. A **3**, 10005 (2015)
12. G.C. Psarras, Composites A **37**, 1545 (2006)
13. C. Wu, X. Huang, X. Wu, J. Yu, L. Xie, P. Jiang, Compos. Sci. Technol. **72**, 521 (2012)
14. W. Liu, J. Chen, D. Zhou, X. Liao, M. Xie, R. Sun, Polym. Chem. **8**, 725 (2017)
15. C. Yang, Y. Lin, C.W. Nan, Carbon **47**, 1096 (2009)
16. Z.M. Dang, M.S. Zheng, J.W. Zha, Small **12**, 1688 (2016)
17. N.A. Almeida, P.M. Martins, S. Teixeira, J.A. Lopes da Silva, V. Sencadas, K. Kühn, G. Cuniberti, S. Lanceros-Mendez, P.A.A.P. Marques, J. Mater. Sci. **51**, 6974 (2016)
18. S. Liu, M. Tian, L. Zhang, Y. Lu, T.W. Chan, N. Ning, J. Mater. Sci. **51**, 2616 (2015)
19. L. Yao, Z. Pan, S. Liu, J. Zhai, H.H.D. Chen, ACS Appl. Mater. Interfaces **8**, 26343 (2016)
20. H. Tang, H.A. Sodano, Appl. Phys. Lett. **102**, 063901 (2013)
21. K. Yu, Y. Niu, Y. Zhou, Y. Bai, H. Wang, J. Am. Ceram. Soc. **96**, 2519 (2013)
22. S. Liu, J. Wang, B. Shen, J. Zhai, Ceram. Int. **43**, 585 (2017)
23. C. Zou, D. Kushner, S. Zhang, Appl. Phys. Lett. **98**, 082905 (2011)
24. X. Zhang, S. Zhao, F. Wang, Y. Ma, L. Wang, D. Chen, C. Zhao, W. Yang, Appl. Surf. Sci. **403**, 71 (2017)
25. T. Wang, X.H. Zhang, D. Chen, Y.H. Ma, L. Wang, C.W. Zhao, W.T. Yang, Appl. Surf. Sci. **356**, 232 (2015)

26. P. Kim, N.M. Doss, J.P. Tillotson, P.J. Hotchkiss, M.J. Pan, S.R. Marder, J. Li, J.P. Calame, J.W. Perry, ACS Nano **3**, 2581 (2009)
27. S. Liu, J. Zhai, J. Wang, S. Xue, W. Zhang, ACS Appl. Mater. Interfaces **6**, 1533 (2014)
28. S. Luo, Y. Shen, S. Yu, Y. Wan, W.H. Liao, R. Sun, C.P. Wong, Energy Environ. Sci. **10**, 137 (2017)
29. C. Zhang, Q. Chi, L. Liu, Y. Chen, J. Dong, T. Ma, X. Wang, Q. Lei, J. Mater. Sci.: Mater. Electron. **28**, 2502 (2016)
30. J. Wang, X. Chao, G. Li, L. Feng, K. Zhao, J. Mater. Sci.: Mater. Electron. **28**, 5435 (2016)
31. X. Zhang, Y. Shen, Q. Zhang, L. Gu, Y. Hu, J. Du, Y. Lin, C.-W. Nan, Adv. Mater. **27**, 819 (2015)
32. S. Liu, J. Wang, B. Shen, J. Zhai, H. Hao, L. Zhao, J. Alloys Compd. **696**, 136 (2017)
33. Z. Pan, L. Yao, J. Zhai, D. Fu, B. Shen, H. Wang, ACS Appl. Mater. Interfaces **9**, 4024 (2017)
34. X. Lin, P. Hu, Z. Jia, S. Gao, J. Mater. Chem. A **4**, 2314 (2016)
35. Z. Pan, J. Zhai, B. Shen, J. Mater. Chem. A **5**, 15217 (2017)
36. S. Liu, S. Xue, B. Shen, J. Zhai, Appl. Phys. Lett. **107**, 032907 (2015)
37. X. Zhang, Y. Shen, B. Xu, Q. Zhang, L. Gu, J. Jiang, J. Ma, Y. Lin, C.W. Nan, Adv. Mater. **28**, 2055 (2016)
38. J.C. Wang, Y.C. Long, Y. Sun, X.Q. Zhang, H. Yang, B. Lin, Appl. Surf. Sci. **426**, 437 (2017)
39. Z.M. Dang, J.K. Yuan, S.H. Yao, R.J. Liao, Adv. Mater. **25**, 6334 (2013)